

See discussions, stats, and author profiles for this publication at: <https://www.researchgate.net/publication/2457617>

A Novel Monte Carlo Algorithm for Simulating Strongly Associating Fluids: Applications to Water, Hydrogen Fluoride, and Acetic Acid

ARTICLE *in* THE JOURNAL OF PHYSICAL CHEMISTRY B · JULY 2000

Impact Factor: 3.3 · DOI: 10.1021/jp001952u · Source: CiteSeer

CITATIONS

107

READS

55

A Novel Monte Carlo Algorithm for Simulating Strongly Associating Fluids: Applications to Water, Hydrogen Fluoride, and Acetic Acid

Bin Chen and J. Ilja Siepmann*

Department of Chemistry and Department of Chemical Engineering and Materials Science,
University of Minnesota, 207 Pleasant Street SE, Minneapolis, Minnesota 55455-0431

Received: May 30, 2000

A novel aggregation-volume-bias Monte Carlo (AVBMC) algorithm is presented which greatly enhances the efficiency of sampling the phase space of fluid systems consisting of strongly associating molecules. The algorithm is compared to the bond-bias Monte Carlo algorithm by Tsangaris and de Pablo (*J. Chem. Phys.* **1994**, *101*, 1477) and the monomer-addition-subtraction algorithm by Visco and Kofke (*J. Chem. Phys.* **1999**, *110*, 5493). The AVBMC algorithm is easy to implement, generally applicable, and robust. Its efficiency is demonstrated for a large variety of processes and systems, including the vaporization of a liquid methane droplet or a water cluster, an investigation of the temperature- and pressure-dependent properties of superheated hydrogen fluoride vapor, and the vapor–liquid coexistence curve of acetic acid.

1. Introduction

Strongly associating fluids are an important class of systems featuring intermolecular attractions with deep (i.e., a few tens of kJ/mol or thousands of Kelvin in thermal units), but narrow wells usually caused by the formation of intermolecular hydrogen bonds. These systems exhibit large deviations from the ideal-gas behavior for their saturated vapor phases due to the formation of aggregates.¹ Typical examples are organic acids, alcohols, and other molecules that are capable of hydrogen bonding. For a long time, the nonideal behavior of such systems had been explained using a “chemical” point of view, that is, in terms of the formation of new chemical species, and the forces between molecules were considered in terms of the formation of “chemical” bonds. However, more recently, the development of improved theoretical and computational treatments for such fluids has shifted the emphasis back to the “physical” nature of association, that is, the intermolecular forces that are usually represented by strongly attractive and oriented electrostatic interactions.

Molecular simulations are, in principle, able to provide an exact connection between a given microscopic model and its macroscopic properties.² Whereas the accuracy of the simulation results depends on the approximations that are made in the force field used to mimic the true physical system, the precision of the simulation results depends solely on the extent to which the phase space of the system is sampled throughout the simulation. In practice, the finite length of the simulations might lead to inadequate sampling of the relevant regions of phase space caused by bottlenecks or traps in phase space.² In particular for strongly associating fluids, the “bonded” configurations result in traps, i.e., configurations that have a very large Boltzmann weight associated with the large favorable energies of cluster formation. However, these “bonded” configurations represent only a small fraction of the total phase space compared to the large number of nonbonded configurations. Thus an efficient sampling algorithm for strongly associating fluids must be able to find the traps, but should not get trapped by them.

The standard Metropolis Monte Carlo algorithm³ used in most molecular simulations fails for strongly associating fluids,

because it utilizes a symmetric underlying Markov matrix and its acceptance probability is based solely on the Boltzmann weight of the energy difference between the trial and present configurations. The symmetry of the matrix results in low efficiency for locating the few bonded configurations in the vast sea of phase space characterized by nonbonded configurations, and the standard acceptance rule makes the destruction of bonded configurations with their favorable energies a very slow process. To overcome this problem, several groups have introduced biased algorithms^{4–8} which are all based on modifications of the underlying Markov matrix and, correspondingly also, of the acceptance rule (i.e., the biased Markov matrix is designed to favor the formation of bonded configurations, but the bias is corrected by adjusting the acceptance rate). In a recent paper by Visco and Kofke,⁸ the complexities and restrictions of these biased algorithms were discussed in detail. The association-biased Monte Carlo (ABMC) method proposed by Busch et al.^{5,6} involves two-particle displacements and requires the specific determination of bonding regions, making the ABMC algorithm rather complex and dramatically increasing the CPU time per ABMC move compared to a simple translational move. The bond-bias Monte Carlo (BBMC) method proposed by Tsangaris and de Pablo⁴ is much simpler, but is presently limited to systems where at most, one other molecule may be in another’s bonding volume and where this bonding volume is exactly known. Visco and Kofke^{7,8} proposed the monomer-addition-subtraction (MASA) algorithm, which is less efficient but more general than the BBMC algorithm. The MASA algorithm allows also for the simulation of chain-forming molecules, but it is limited to bivalent associating fluids (e.g., hydrogen fluoride) in which linear chains and rings are the dominant bonded configurations, because the MASA algorithm prevents the formation of branched aggregates.^{7,8}

In the next section, the aggregation-volume-bias Monte Carlo (AVBMC) algorithm is presented. This algorithm attempts to alleviate some of the shortcomings of the other biased algorithms. In section 3, the molecular models (force fields) and simulation details of this study are briefly described. The AVBMC algorithm was tested for a plethora of different scenarios, including the vaporization of a liquid methane droplet or a water cluster, the superheated-vapor phase of hydrogen fluoride, and the vapor–liquid phase equilibria of acetic acid.

* Corresponding author E-mail: siepmann@chem.umn.edu.

The results of these simulations are presented and discussed in section 4, and section 5 provides concluding remarks.

2. The Aggregation-Volume-Bias Monte Carlo Algorithm

To simplify the description of the AVBMC algorithm, we present it here in terms of simulations in the canonical ensemble. In this case, the AVBMC algorithm introduces a novel trial move that may be called an intrabox swap move (in analogy with the particle swap moves employed in grand canonical and Gibbs ensemble simulations). This intrabox swap move is targeted at sampling the formation (growth) or destruction (shrinkage) of aggregates, whereas conventional translational (and, if needed, rotational and conformational) trial moves are used to explore nearby regions of phase space.

For comparison, we begin with a brief sketch of an unbiased translational move. Starting from a given configuration of the system, state *A*, the Metropolis translational move proceeds as follows: (1) Randomly select a particle *i*. (2) Attempt a displacement of particle *i* leading to the trial configuration, state *B*, where the displacement vector is randomly selected from a uniform distribution bounded by a maximum allowed translational displacement. (3) Calculate the potential energy difference, $\Delta E = E_B - E_A$, and accept this move with a probability of

$$\text{acc}(A \rightarrow B) = \min[1, \exp(-\Delta E/k_B T)] \quad (1)$$

where k_B and T are Boltzmann's constant and the absolute temperature, respectively. It is then straightforward to demonstrate that the Metropolis scheme satisfies the condition of microscopic reversibility²

$$\rho_A \times \alpha(A \rightarrow B) \times \text{acc}(A \rightarrow B) = \rho_B \times \alpha(B \rightarrow A) \times \text{acc}(B \rightarrow A) \quad (2)$$

because a symmetric underlying Markov matrix (here, uniform transition probability) is used, such that $\alpha(A \rightarrow B) = \alpha(B \rightarrow A)$, and the probability density, ρ , of any given state is proportional to its Boltzmann weight.⁹ The Metropolis scheme, however, is clearly not efficient for hopping between bonded and nonbonded configurations as required for strongly associating fluids. First, because of the small volume of phase space that the bonded configurations occupy (compared to the total volume of phase space), the probability of attempting a move that goes from a nonbonded configuration to a bonded one is very low. Second, once a bonded configuration is found, any trial move resulting in the destruction of the bonded configuration has a very low acceptance rate because of the large energy difference between these two states. Thus, during a Metropolis Monte Carlo simulation for a system of strongly associating fluids, the phase space trajectory might either miss forming bonded configurations or get trapped once a bonded configuration is found. Therefore sampling phase space well enough to be able to calculate reliable ensemble averages will require an exceedingly long simulation time (i.e., a high number of Monte Carlo steps).

The problem with the Metropolis sampling scheme is evident, and the general direction for solving this problem is also obvious:² increase the transition probability for moves that lead to the formation of bonded configurations, and enhance the acceptance rate for moves that lead to the destruction of bonded configurations. Starting from a given configuration *A*, an AVBMC trial move proceeds as follows: (1) Randomly select a particle *i* to be swapped. (2) Randomly select a second particle *j* (with $j \neq i$) that acts as the target for the swap move. (3) With a probability of P_{bias} , molecule *i* is allowed to swap only into

the bonded region of molecule *j*, called the B_{in} state,¹⁰ while with a probability of $1 - P_{\text{bias}}$ the molecule *i* is swapped into the nonbonded region of molecule *j*, called the B_{out} state (see the Appendix for a description of how to efficiently select trial sites that are in the *in* or *out* regions). (4) Calculate the potential energy difference, $\Delta E = E_B - E_A$. (5) Accept this move with the following set of acceptance probabilities:

(a) For the two cases in which the swap move does not involve particle *i* entering or leaving the bonded region of particle *j*—that is, the cases *out* \rightarrow *out* or *in* \rightarrow *in*—the standard Metropolis acceptance rule (see eq 1) is used.

(b) If the move results in the formation of a bonded configuration of *i* and *j* (irrespective of whether *i* was bonded to another particle *k* before the move)—that is, the *out* \rightarrow *in* case—the following acceptance rule is used:

$$\text{acc}(A_{\text{out}} \rightarrow B_{\text{in}}) = \min \left[1, \frac{(1 - P_{\text{bias}}) \times V_{\text{in}} \times \exp(-\Delta E/k_B T)}{P_{\text{bias}} \times V_{\text{out}}} \right] \quad (3a)$$

where V_{in} is the volume of the bonded *in* region and $V_{\text{out}} = V - V_{\text{in}}$ is the remainder of the system's volume.

(c) If the move results in the destruction of a bonded configuration of *i* and *j* (irrespective of whether the swap move places *i* in the bonded region of another particle *k*)—that is, the *in* \rightarrow *out* case—the following acceptance rule is used:

$$\text{acc}(A_{\text{in}} \rightarrow B_{\text{out}}) = \min \left[1, \frac{P_{\text{bias}} \times V_{\text{out}} \times \exp(-\Delta E/k_B T)}{(1 - P_{\text{bias}}) \times V_{\text{in}}} \right] \quad (3b)$$

The bias introduced in the underlying Markov matrix α is proportional to $P_{\text{bias}}/V_{\text{in}}$ for trials that are placed in the *in* region (irrespective of whether the old state is in the *in* or the *out* region) and proportional to $(1 - P_{\text{bias}})/V_{\text{out}}$ for trials that are placed in the *out* region (irrespective of whether the old state is in the *in* or the *out* region). Inserting the bias of the underlying Markov matrix and the acceptance rules (eqs 1, 3a, and 3b) into eq 2 demonstrates that the detailed balance condition is satisfied for all four cases (*out* \rightarrow *out*, *in* \rightarrow *in*, *in* \rightarrow *out*, and *out* \rightarrow *in*).

Similar to the other biased algorithms, the underlying Markov matrix for the AVBMC algorithm is asymmetric. In this case, the transition probability of attempting a move that creates a bonded configuration can be increased by adjusting the values of P_{bias} and V_{in} . Correspondingly, the acceptance probability for a move that destroys a bonded configuration is enhanced. Therefore, the AVBMC algorithm greatly improves the rate of bond formations and destructions, thereby facilitating the efficient sampling of phase space for strongly associating fluid systems. It is important to note here that in deriving the AVBMC algorithm, we did not have to specify either the details of the molecular model (e.g., association controlled by square-well or Coulombic interactions) or the type of bonded aggregates (e.g., dimers, linear chains, rings, or branched structures). This fact points to the general applicability of the AVBMC algorithm. In addition, the AVBMC algorithm has essentially no computational overhead. The only overhead comes from the selection of the second particle, the determination of whether particle *i* is *in* or *out* of the bonded region of particle *j* before the move (requiring the calculation of only *one* distance), and from the identification of trial sites that are in the selected *in* or *out* volumes (see the Appendix). Because none of these costs depend on the system size (i.e., the number of interaction sites), the overhead is negligible for all practical cases.

In comparison, the biased algorithms previously proposed for simulating strongly associating fluids^{4–8} are rather complex and often are limited to certain situations. The BBMC algorithm developed by Tsangaris and de Pablo⁴ depends on the use of special molecular models. These models exclude the possibility that more than one molecule may be in another's bonding volume; thus they allow only for monomer and dimer states. The MASA scheme developed by Visco and Kofke^{7,8} also relies on a specific model that allows only for the formation of linear chains or rings. Thus, problems might occur in the MASA algorithm if a conventional translational move resulted in the formation of a branched aggregate. A relatively large computational overhead is associated with the MASA algorithm, e.g., one needs to keep track of all the oligomers (aggregates) and their ends, assign each molecule to a specific oligomer (even after a conventional translational move), and, in the subtraction move, repeat the repositioning of the subtracted segment until the segment is placed as a monomer.

Finally, because the AVBMC move may be viewed as a special intrabox swap,^{11,12} its efficiency can be further improved by combining it with more advanced techniques for particle swaps. Such techniques include multiple insertions of the first bead of the trial molecule^{13,14} and configurational-bias Monte Carlo methods^{15–19} to deal with more complex molecular systems. The only shortcoming of the AVBMC algorithm is that we do not specify whether particle *i* is associated with particles other than *j*. Thus during the *out* → *in* process, although *i* is *out* of the bonding volume with *j*, it nevertheless may not be a monomeric species. To avoid this problem, however, one would need to keep track of all clusters at all times, which would greatly increase the computational overhead.

3. Molecular Models and Simulation Details

For all systems studied here, the nonbonded intermolecular interactions are described by pairwise-additive Lennard-Jones (LJ) 12–6 potentials and Coulombic interactions of partial charges

$$u(r_{ij}) = 4\epsilon_{ij} \left[\left(\frac{\sigma_{ij}}{r_{ij}} \right)^{12} - \left(\frac{\sigma_{ij}}{r_{ij}} \right)^6 \right] + \frac{q_i q_j}{4\pi\epsilon_0 r_{ij}} \quad (4)$$

where r_{ij} , ϵ_{ij} , σ_{ij} , q_i , and q_j are the separation, LJ well depth, LJ size, and partial charges, respectively, for the pair of atoms *i* and *j*. Lorentz–Berthelot combining rules² were used to determine the parameters for unlike Lennard-Jones interactions.

A. Vaporization of a Liquid Methane Droplet. The TraPPE-UA (Transferable Potentials for Phase Equilibria–United Atom) force field²⁰ was used for methane, with the following LJ parameters for the single interaction site: $\epsilon/k_B = 148$ K and $\sigma = 3.73$ Å. A spherical potential truncation at 14 Å and long-range corrections for the energy were used.² The system consisted of 500 methane molecules and was initialized from the final configuration of a liquid-state simulation that had been equilibrated for more than 10,000 Monte Carlo cycles at a temperature of 100 K ($\rho = 0.410$ g/mL using a periodic simulation box with a linear dimension of 31.9 Å). Thereafter, this liquid droplet (having a cubic shape) was put into a much larger periodic box with a linear dimension of 270 Å, resulting in a density of 0.000677 g/mL, just below the saturated vapor density for this model. Simulations in the canonical ensemble were then carried out ($T = 100$ K), and the evolution of the properties during vaporization and those of the equilibrated vapor were investigated.

B. Vaporization of a Water Cluster. The extended simple point-charge (SPC/E) water model developed by Berendsen et

al.²¹ was used. This three-site model is fully rigid, with an O–H bond length of 1.0 Å and a H–O–H bond angle of 109.47°. Besides one Lennard-Jones site on the oxygen ($\epsilon/k_B = 78.2$ K and $\sigma = 3.1655$ Å), there are two partial charge sites on the hydrogens with $q = 0.4238$ e and one additional charge site on the oxygen with $q = -0.8476$ e. A spherical potential truncation at an oxygen–oxygen distance of 30 Å was used for molecule–molecule interactions, and long-range corrections were applied only for the LJ interactions. A deep local minimum for a 20-molecule cluster was found using the simulated annealing method. The structure of this local minimum was cylindrical with four layers of cyclic pentamers. This 20-molecule cluster was then put in a periodic box with a linear dimension of 370 Å ($\rho = 0.0000118$ g/mL) and left to vaporize at 298 K.

C. Superheated Hydrogen Fluoride Vapor. The hydrogen fluoride molecules were represented by the rigid, three-site OPLS (optimized potentials for liquid simulation) model.²² The H–F bond length is 0.917 Å, and an additional charge site is placed 0.166 Å from the fluorine toward the hydrogen along the H–F bond axis. One Lennard-Jones site is located at the fluorine with $\epsilon/k_B = 75.75$ K and $\sigma = 2.984$ Å. There are equal partial charges of +0.725 e on both the fluorine and hydrogen sites, and a compensating negative charge at the additional charge site. Because we will compare our work directly to previous simulations by Visco and Kofke,⁷ we followed their prescription (which is identical to that used in ref 22) of a molecule-based spherical potential truncation at a fluorine–fluorine separation of 8 Å, as well as the use of long-range corrections for only the LJ part of the potential. The system consisted of 108 hydrogen fluoride molecules. The initial configuration was constructed using a layered crystal structure. Isobaric–isothermal Monte Carlo simulations²³ were performed over a range of pressures and temperatures using 5×10^4 and 10^6 Monte Carlo cycles for the equilibration and production periods at each state point (one Monte Carlo cycle consists of $N = 108$ Monte Carlo moves).

D. Vapor–Liquid Coexistence Curve for Acetic Acid. The acetic acid molecules were represented by the semiflexible OPLS united-atom model,²⁴ in which the methyl group is treated as a pseudoatom. The LJ parameters and partial charges of the five sites are as follows: $\epsilon/k_B = 80.6$ K, $\sigma = 3.91$ Å, and $q = +0.08$ e (for CH₃); 52.9 K, 3.75 Å, and +0.55 e (for C); 105.7 K, 2.96 Å, and –0.50 e (for =O); 85.6 K, 3.00 Å, and –0.58 e (for –O–); and +0.45 e (for H). For the LJ part of the potential, a spherical cutoff radius of 14 Å was utilized with standard long-range corrections for the energy, pressure, and chemical potential, whereas an Ewald sum with tinfoil boundary conditions ($\kappa \times L = 5$ and $K_{\max} = 5$) was used for the long-range electrostatic part of the potential.

The atoms were connected by bonds with fixed lengths of 1.52, 1.364, 1.214, and 0.97 Å for (CH₃)–C, C–O, C=O, and O–H, respectively. Bond-angle bending was governed by harmonic potentials

$$u_{\text{bend}} = \frac{1}{2} k_\theta (\theta - \theta_0)^2 \quad (5)$$

with force constants of $k_\theta/k_B = 80\,600$ K rad^{–2} (C–C=O and O=C–O), 35 200 K rad^{–2} (C–O–H), and 70 600 K rad^{–2} (C–C–O). The corresponding equilibrium bond angles θ_0 were set to 126, 123, 107, and 111°, respectively. The motion of the dihedral angles ϕ was controlled by the OPLS united-atom torsional potential²⁴

$$u_{\text{tors}} = c_1 [1 + \cos(\phi + f_1)] + c_2 [1 - \cos(2\phi)] \quad (6)$$

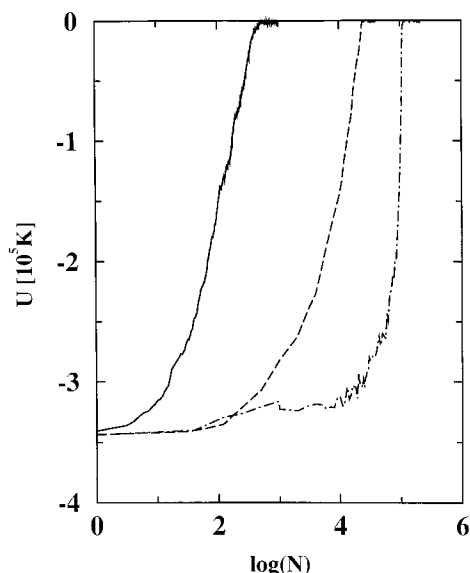


Figure 1. Evolution of the internal energy versus the number of Monte Carlo cycles for the vaporization of the Lennard-Jones droplet. Results are shown for the simulations using only translational moves (dashed-dotted line), using only unbiased swap moves (dashed line), and using only AVBMC moves (solid line).

with $c_1/k_B = 630.0$ K and $c_2/k_B = 1562.4$ K for both OCOH and CCOH, but $f_l = 180^\circ$ for OCOH and $f_l = 0^\circ$ for CCOH.

A combination of the Gibbs ensemble Monte Carlo method (GEMC)^{25,26} and the coupled-decoupled configurational-bias Monte Carlo algorithm (CBMC)¹⁸ was employed to study the vapor-liquid phase equilibria. The system consisted of 400 acetic acid molecules. Its initial configuration was constructed using a layered crystal structure which was melted for about 500 Monte Carlo cycles at $T = 3000$ K, followed by 4000 cycles of cooling at 500 K. During the melting process, only translational, rotational, and configurational-bias moves were performed, while volume exchange moves were added during the cooling process. During the GEMC simulations, the molecules were allowed to exchange between the vapor and liquid phases using coupled-decoupled CBMC swap moves. In addition, particles were swapped *within* the vapor phase using AVBMC moves. Simulations were carried out over the temperature range from 300 to 650 K. These GEMC simulations were equilibrated for at least 10^4 Monte Carlo cycles, and the production runs consisted of more than 5×10^4 Monte Carlo cycles.

4. Results and Discussion

A. Vaporization of a Liquid Methane Droplet. The vaporization of the methane droplet was followed with three different simulation algorithms: (1) using only translational moves (to optimize the efficiency of these moves, the maximum displacement was adjusted every 2000 Monte Carlo cycles to yield an acceptance rate of 50%); (2) using intrabox swaps without additional bias; and (3) using the AVBMC algorithm. In the third simulation, the bonded or *in* region around the target particle was defined by a spherical shell with minimum and maximum pair distances of 3 and 20 Å, respectively. The inner-shell distance of 3 Å was chosen based on the σ value of 3.73 Å for the methane particles, and the outer-shell distance of 20 Å reflected the size of the initial liquid methane droplet. P_{bias} was set to 0.5, and no attempt was made to further optimize P_{bias} and V_{in} .

The energy evolution of the methane system after placement in the larger simulation box is plotted in Figure 1. It is evident that the AVBMC algorithm leads to a dramatic increase in the

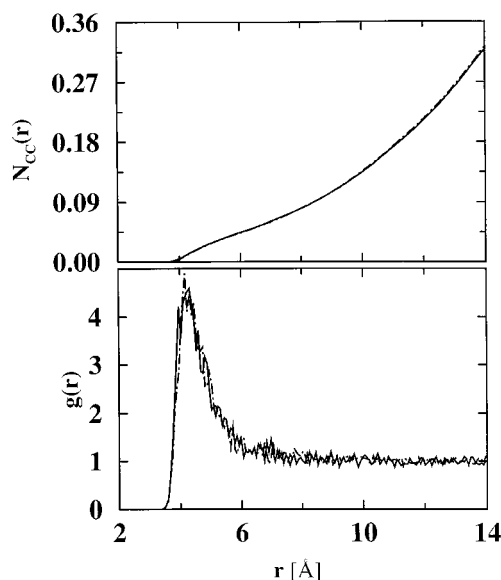


Figure 2. Methane-methane radial distributions (bottom) and number integrals (top). Results for the equilibrated portion of the runs are shown for the simulations using only translational moves (dashed-dotted lines) and using only AVBMC moves (solid lines).

equilibration (i.e., vaporization) rate of the methane droplet. In fact, it took only 500 Monte Carlo cycles with the AVBMC algorithm to fully vaporize the methane droplet, whereas 2.5×10^4 and more than 10^5 cycles were required when unbiased swap moves or translational moves, respectively, were used.

Although the equilibration rate is obviously improved with the use of the AVBMC algorithm, it is equally important to demonstrate that the equilibrium properties of the methane vapor are sampled correctly using only AVBMC moves. Using an additional 10^4 Monte Carlo cycles after equilibration, we found the average energies of the vapor to be 0.0203 ± 0.0005 , 0.0204 ± 0.0003 , and 0.0204 ± 0.0004 kJ/mol for the simulations using only AVBMC, unbiased swap, and translational moves, respectively. The methane-methane radial distribution functions (RDFs) and the corresponding number integrals are compared in Figure 2. The very good agreement among the three simulation runs demonstrates that the AVBMC algorithm indeed yields the correct ensemble averages.

B. Vaporization of a Water Cluster. Four simulations employing different types of Monte Carlo moves were performed to study the vaporization of the 20-molecule water cluster (see Figure 3). First, a simulation using only the standard translational and rotational moves (the type of move is selected randomly with equal probabilities) was carried out. The maximum displacements for these moves were optimized to yield a 50% acceptance rate. The standard moves quickly supplied thermal energy to the water cluster, but it took more than 3×10^6 Monte Carlo cycles before the cluster began to break, and an equilibrated vapor state was reached only after approximately 4×10^6 cycles. Second, CBMC intrabox swaps without volume bias (and with 20 different trial orientations generated for the rigid molecule) were used in addition to the standard translational and rotational moves (again the type of move is selected randomly). In this case, equilibration was observed after about 3×10^5 Monte Carlo cycles, a reduction of about 1 order of magnitude compared to the simulation that used only translational and rotational moves. However, a large part of this gain is compensated for by the increased cost of the CBMC swap move. Using a split-energy technique²⁷ with center-of-mass-based cutoff for the CBMC part²⁰ results in an

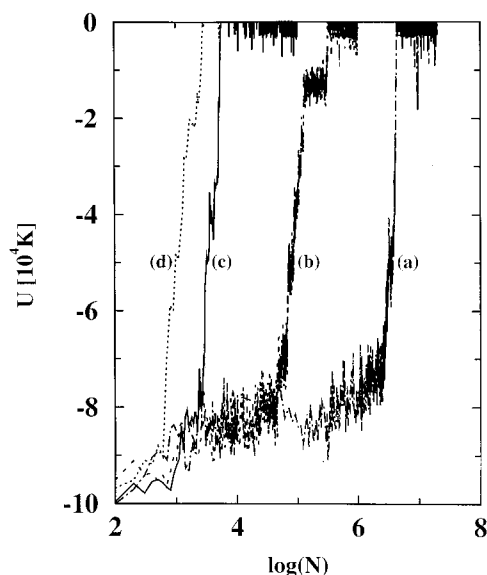


Figure 3. Evolution of the internal energy versus the number of Monte Carlo cycles for the vaporization of the 20-molecule water cluster. Results are shown for the simulations using only translational and rotational moves (a); using translational, rotational, and CBMC swap moves without volume bias (b); using translational, rotational, and AVBMC moves without multiple-first-bead insertions and $2.5 \text{ \AA} \leq r_{\text{in}} < 5.0 \text{ \AA}$ (c); and with multiple-first-bead insertions and $2.5 \text{ \AA} \leq r_{\text{in}} < 3.5 \text{ \AA}$ (d).

increase in the computational cost for the CBMC swap move that is higher by a factor of 5 than for a translational move.

Third, a simulation using AVBMC moves, translations, and rotations was carried out. The bonded region was defined by an oxygen–oxygen pair distance in the range between 2.5 and 5 Å according to the hydrogen-bond distance, and P_{bias} was set to 0.5. After the oxygen site of the trial molecule was placed, CBMC was used to find suitable positions for the two hydrogen atoms (with 20 different trial orientations generated for the rigid molecule). The equilibration period for this simulation was reduced to 6×10^3 Monte Carlo cycles, a gain of a factor of 50 compared to the CBMC swap moves without volume bias.

Finally, the convergence rate could be improved even further by adjusting the range of the bonded region and by adding multiple-first-bead insertions during the AVBMC moves. In particular, when a bonded region with an oxygen–oxygen separation in the narrower range between 2.5 and 3.5 Å (a distance that coincides with the first minimum in the oxygen–oxygen RDF of liquid water) and 10 trial sites for the insertion of the oxygen site were used, the water cluster was equilibrated in less than 3000 Monte Carlo cycles. Although the computational overhead of this simulation was larger (by factors of approximately 1.5, 1.6, and 8 compared to the simulations using AVBMC without multiple-first-bead insertions, using swap moves without volume bias, and using only translational and rotational moves), this is still the most efficient simulation of the four. Obviously, the standard translational and rotational moves are not suitable for the sampling of water vapor at room temperature.

C. Superheated Hydrogen Fluoride Vapor. Hydrogen fluoride (HF) is the prototypical example of a chain-forming associating fluid because it has only one donor site for hydrogen bonding. In addition, ab initio calculations by Suhm²⁸ indicated that branching is unimportant for HF oligomers at low densities, such as those found in its vapor phase. The superheated vapor phase of HF was previously investigated by Visco and Kofke using the MASA algorithm,⁷ and the temperature dependencies

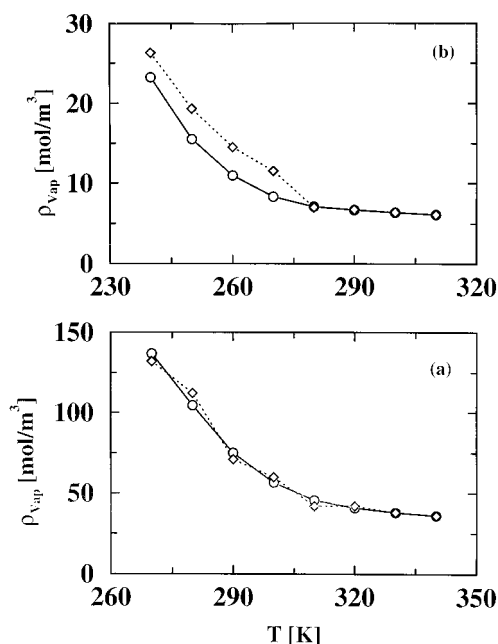


Figure 4. Density versus temperature for the superheated hydrogen fluoride vapor at 15.5 kPa (top) and at 96.1 kPa (bottom). Diamonds denote the results by Visco and Kofke obtained with the MASA algorithm,⁷ and circles denote the AVBMC simulations of this work. Lines are drawn only as guides for the eye.

of the density, heat capacity, and oligomer distribution were studied along three low-pressure isobars. Using the AVBMC algorithm, we repeated the calculations for the 15.5 and 96.1 kPa isobars using the HF model of Cournoyer and Jorgensen.²² However, it should be noted here that the production periods of our calculations were about 1 order of magnitude longer than those of Visco and Kofke (10^6 versus 9.3×10^4 Monte Carlo cycles). The bonded V_{in} region was bounded by an inner shell at 2.0 Å and an outer shell at 5.0 Å based on the F–F separation, and P_{bias} was set to 0.5. Ten trial sites were considered for the multiple-first-bead insertion of the fluorine atom, and 10 molecular orientations were used for the CBMC growth of the remainder of the linear molecule.

The densities of the superheated HF vapor are plotted as function of temperature in Figure 4. Although the agreement between our calculations and those by Visco and Kofke⁷ is good over the entire temperature range for the isobar at $p = 96.1$ kPa, there are noticeable deviations at the lower temperatures (≤ 270 K) for the 15.5 kPa isobar. In general, the curves for the AVBMC simulations are smoother, which should come as no surprise considering that the production periods for these simulations were much longer. The running averages of the density for our simulations at the four lowest temperatures on the 15.5 kPa isobar are shown in Figure 5. Apparently as many as 5×10^5 Monte Carlo cycles were required to converge the density in some cases.

The heat capacity can be calculated either from finite differences between simulations at adjacent temperatures or using the fluctuation formula.⁹ As the calculations of fluctuation properties converge very slowly and require a sufficient exploration of phase space,² we followed the lead of Visco and Kofke⁷ and used the fluctuation formula to calculate the heat capacity to demonstrate the sampling efficiency of the AVBMC algorithm. The constant-pressure heat capacities obtained from the MASA⁷ and the AVBMC simulations are compared in Figure 6. First of all, both calculations agree quite well with respect to the peak positions, heights, and widths for both isobars. For

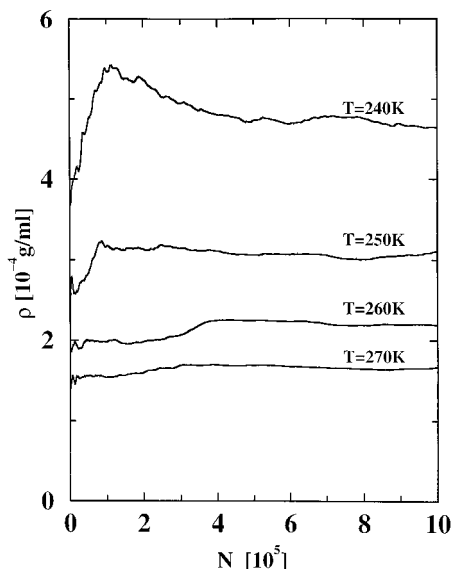


Figure 5. Density convergence plots (running averages versus the number of Monte Carlo cycles) obtained with the AVBMC algorithm for the 15.5 kPa isobar at $T = 240, 250, 260$, and 270 K.

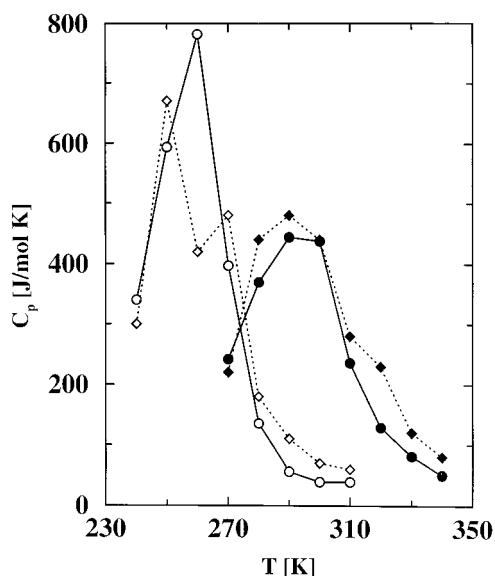


Figure 6. Constant-pressure heat capacity versus temperature for the superheated hydrogen fluoride vapor at $p = 15.5$ kPa (open symbols) and 96.1 kPa (filled symbols). Diamonds and circles denote the MASA and AVBMC results as in Figure 4.

the 15.5 kPa isobar, the peak is found at $T = 260$ K with a magnitude of about 780 J/mol K, whereas it is shifted to $T = 290$ K with a magnitude of about 440 J/mol K for the 96.1 kPa isobar. As observed also by Visco and Kofke,⁷ agreement with the experimental data²⁹ is less satisfactory, especially with respect to the peak magnitude. The heat capacities calculated from the AVBMC simulations are, in general, slightly lower than those obtained from the MASA simulations. Again, the curves for the longer AVBMC simulations are smoother. This is most evident for 250 – 270 K region of the 15.5 kPa isobar, where the shorter MASA simulations might not have converged.

The running averages of the heat capacity for the four lowest temperatures ($T \leq 270$ K) of the 15.5 kPa isobar are shown in Figure 7. Compared to those of the density (Figure 5), the running averages of the heat capacity had more and bigger jumps. The convergence rate for the heat capacity is related to the autocorrelation length of the fluctuations in the internal

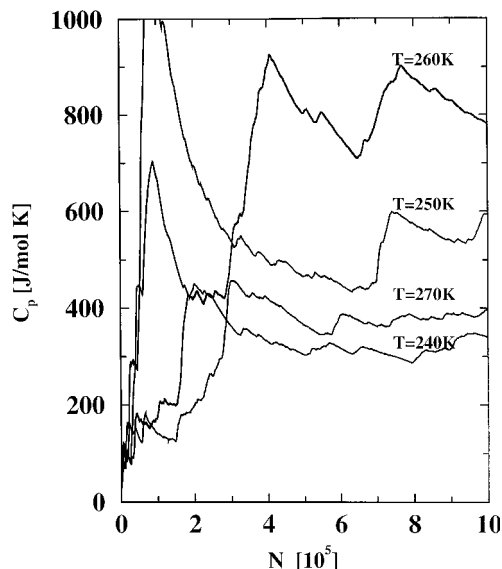


Figure 7. Constant-pressure heat capacity convergence plots (running averages versus the number of Monte Carlo cycles) for the 15.5 kPa isobar at $T = 240, 250, 260$, and 270 K.

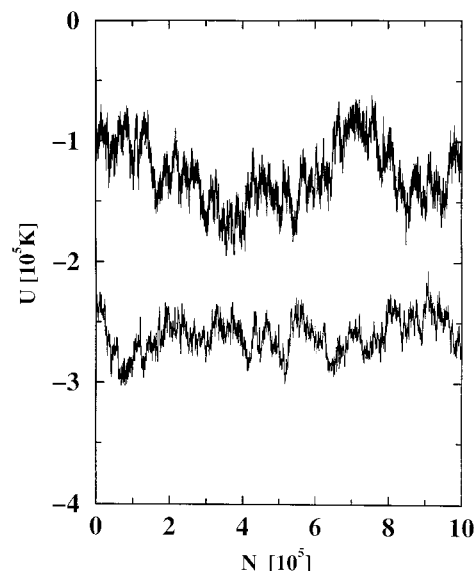


Figure 8. Internal energy fluctuation plots for the 15.5 kPa isobar at $T = 240$ K (lower curve) and 260 K (upper curve).

energy (see Figure 8). In particular, at $T = 260$ K we observe large-scale energy fluctuations that are separated by more than 3×10^5 Monte Carlo cycles. For example, the energy evolution changes sign at about 4×10^5 Monte Carlo cycles (a minimum) and at about 7.5×10^5 Monte Carlo cycles (a maximum). These changes result in peaks in the heat capacity evolution. At present, we have not determined the structural changes at the microscopic level that correspond to these large-scale energy fluctuations. However, these large-scale fluctuations make it impossible to determine reliable statistical errors for the heat capacity even for the rather long AVBMC simulations.

Although the AVBMC algorithm greatly enhances the sampling of the addition or removal of a single molecule to or from a given cluster, it is not yet designed to allow for the fusion of two smaller clusters into one larger cluster or the breakup of one larger cluster into two smaller clusters. However, combining AVBMC moves with cluster moves, such as those proposed by Wu et al.³⁰ for the sampling of surfactant aggregates, should overcome this problem.

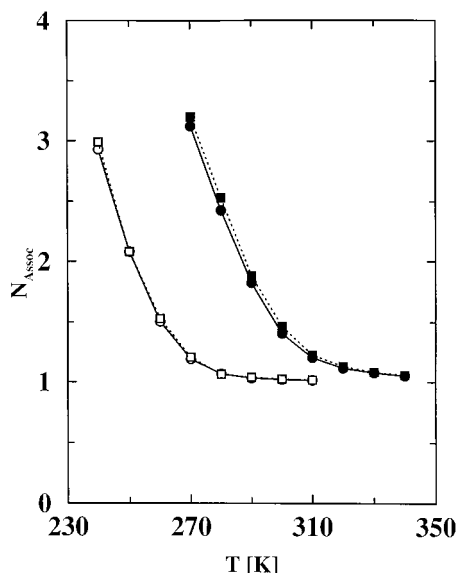


Figure 9. Average association number versus temperature calculated from the inverse compressibility factor (squares) and from determination of the number of clusters using a distance-based criterion (circles). Results for the 15.5 and 96.1 kPa isobars are shown as open and filled symbols, respectively.

The distribution of cluster sizes (aggregation numbers) and types (linear, cyclic, or branched) is one of the most important properties in the description of strongly associating fluids. Whereas the experimental determination of these microscopic properties is rather difficult, they can be simply calculated from a configuration file generated throughout a simulation. For most of what follows, we have used a simple distance-based criterion to determine whether a molecule is “bonded” to another. The first minimum of the F–F radial distribution function (not shown) at $T = 270$ K and $p = 96.1$ kPa was found at 3.3 Å, and for consistency this distance was used to analyze for clusters at all temperatures and pressures (whereas the position of the minimum in the radial distribution function shifts slightly with temperature and pressure). Using this criterion, an average association number can be calculated from the ratio of the number of HF molecules to the number of clusters. This quantity is plotted against the temperature for both isobars in Figure 9.

In addition, one could also follow a macroscopic route and estimate the average association number from the inverse compressibility factor (also shown in Figure 9); that is, assuming an ideal gas of average-size clusters. As expected, the average association numbers decrease with increasing temperature and reach a limiting value of unity for both isobars. The microscopic and macroscopic association numbers are in satisfactory agreement, in particular for the 15.5 kPa isobar and at higher temperatures. However, the macroscopic association number is found to be noticeably larger for the lower temperatures of the 96.1 kPa isobar, reflecting deviations from the ideal gas behavior.

In Figure 10, the fractions of free HF molecules (i.e., those that are not associated with any other molecule) are plotted against the temperature for both isobars. As is discussed in more detail by Visco and Kofke,⁷ the rate of change (slope) of this quantity contributes significantly to the heat capacity. Indeed, the heat capacity maximum occurs around the same temperature at which about half of the molecules are monomers and at which the largest slope is observed (Figure 10). Thus the heat capacity maximum is caused by a “phase transition” from a low-

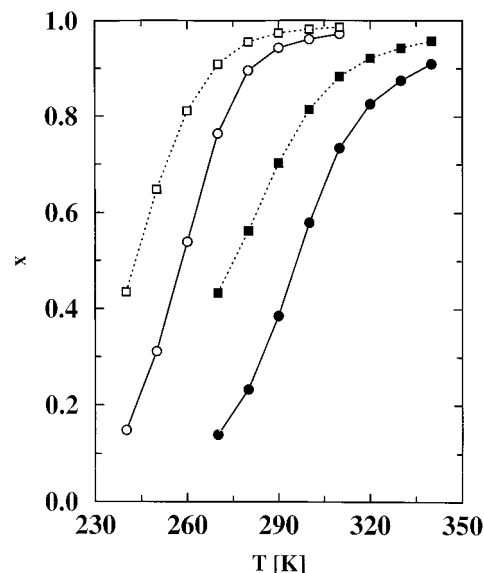


Figure 10. Fraction of nonassociated HF molecules (circles) and fraction of monomeric clusters (squares) versus temperature. Results for the 15.5 and 96.1 kPa isobars are shown as open and filled symbols, respectively.

temperature vapor with clusters as the predominant species to a high-temperature vapor dominated by monomeric HF molecules.

The temperature dependence of the cluster distributions is shown in Figures 10 (for monomeric clusters) and 11 (for larger clusters). These cluster distributions are given as the ratio of the number of clusters of a given size to the total number of clusters, which should not be confused with the fraction of molecules belonging to a cluster of a given size (conversion of the two measures is straightforward). The fraction of clusters of a given size can be used to compute directly the pseudo-equilibrium constants that are input parameters for equations of state that describe the vapor of associating fluids in terms of an equilibrium mixture of clusters.³¹ For both isobars, we observe that the fraction of monomeric clusters increases monotonically with increasing temperature, whereas the fractions of all clusters consisting of four or more HF molecules decrease monotonically with increasing temperature. The noticeable exceptions are the dimeric clusters, which exhibit maxima for both isobars at temperatures close to the peaks in the heat capacity. In addition, the fractions of trimeric clusters show a small maximum at $T = 280$ K for the 96.1 kPa isobar and a flat region for the two lower temperatures of the 15.5 kPa isobar. Visco and Kofke argued that the maxima for the dimeric clusters are an indication that dimeric clusters are an intermediate species in the decomposition of larger clusters.⁷ In agreement with the findings of Visco and Kofke,⁷ it is observed that tetramers and pentamers are the dominant clusters for the low-temperature vapors of HF.

The fractions of molecules belonging to a cluster of a given aggregation number and architecture are plotted in Figure 12 for two state points which are representative for the low-temperature vapor phase of HF. For both state points, the largest fractions of molecules belong to tetramers, pentamers, and monomers (in descending order). The pronounced dips for dimers and trimers are evidence for the importance of cooperativeness in hydrogen-bonding.³² Furthermore, a large degree of cooperativeness requires cyclic structures that maximize the number of hydrogen bonds and that, for larger clusters, require relatively little strain of the hydrogen-bonded network. Thus,

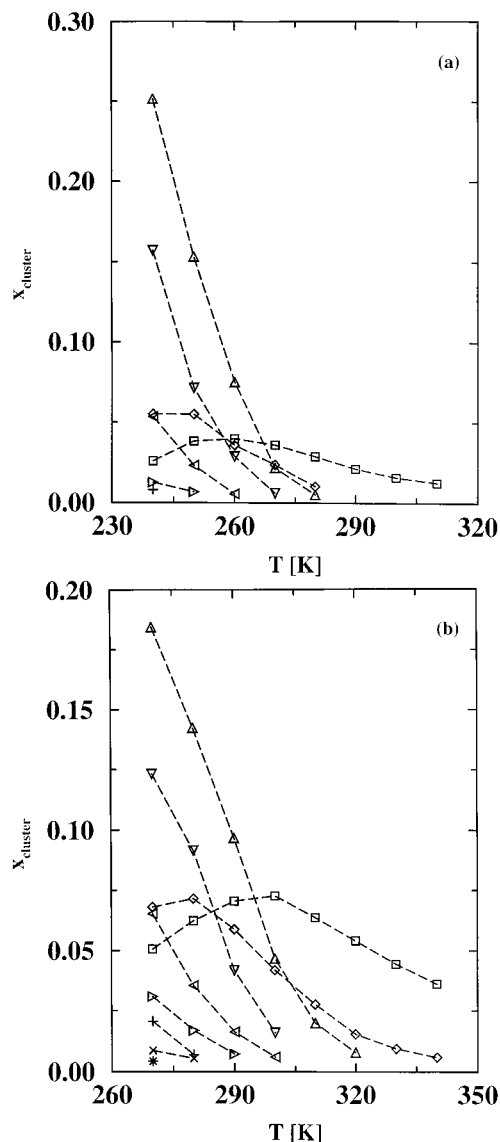


Figure 11. Cluster size distribution versus temperature for the 15.5 kPa isobar (a) and the 96.1 kPa isobar (b). Fractions of dimers, trimers, tetramers, pentamers, hexamers, heptamers, octamers, nonamers, and decamers are depicted by squares, diamonds, triangles up, triangles down, triangles left, triangles right, pluses, crosses, and stars. Fractions are shown only when larger than 0.005.

we also analyzed for the fraction of molecules with respect to cluster architecture.

Three types of cluster architecture were considered: linear, cyclic, and branched. Cluster architecture was assigned by the following rules: (1) If a cluster contains at least one molecule that is bonded to more than two neighbors, then it is branched. (2) If a cluster contains only molecules with exactly two neighbors, then it is a (monocyclic) ring. (3) In all other cases, it is a linear cluster.

In agreement with the cooperative hydrogen-bonding argument, it was observed that cyclic architectures are dominant for clusters containing between three and six molecules. Furthermore, it must be emphasized that branched architectures make an important contribution. About 30% of tetramers and pentamers are branched; it becomes the favored architecture for clusters containing eight or more molecules. On the contrary, linear conformations occur rather infrequently, with the exception of trimers, for which only linear or cyclic architectures are possible (of course, all dimers have to be linear). The obvious

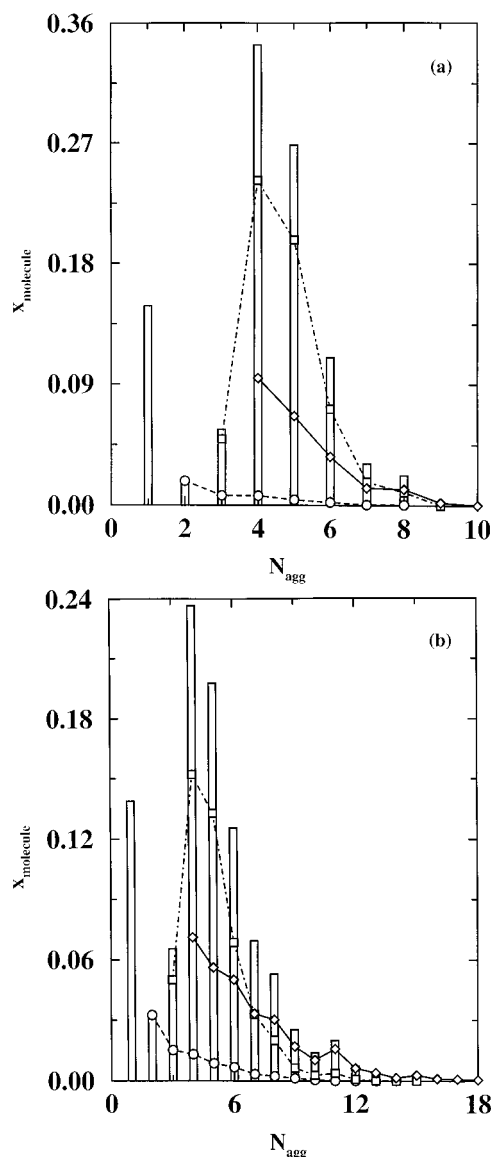


Figure 12. Fraction of molecules belonging to a specific cluster architecture versus the aggregation number for $T = 240$ K and $p = 15.5$ kPa (a) and for $T = 270$ K and $p = 96.1$ kPa (b). Circles, squares, diamonds, and histograms depict the fractions of molecules in linear, cyclic, branched, and in all clusters of a given aggregation number.

explanation for these architectural preferences is that the ring structures are favored by energetic considerations, whereas branched architectures are favored on entropic grounds (there are many branched “isomers”, but only one “isomer” exists for each linear or monocyclic cluster).

Although we cannot answer the question of whether the preference for branched architectures is only an artifact caused by shortcomings of the relatively simple three-site model of Cournoyer and Jorgensen,^{22,28} it is obviously important to sample these architectures. Thus great care needs to be employed when using algorithms such as BBMC⁴ or MASA,⁸ which are specific to certain architectures. Recall that the BBMC algorithm allows only for the formation of dimers, whereas the MASA algorithm prevents the occurrence of branched oligomers.

D. Vapor–Liquid Coexistence Curve for Acetic Acid. The calculation of the vapor–liquid coexistence curve (VLCC) of acetic acid was used by Tsangaris and de Pablo to demonstrate the efficiency of the BBMC algorithm for simulating strongly associating fluids.⁴ However, their Gibbs-ensemble simulations were carried out for a very crude model containing a single LJ

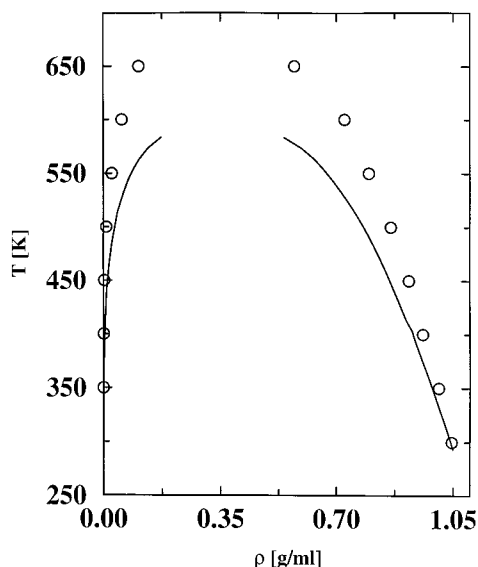


Figure 13. Vapor-liquid coexistence curves for acetic acid. Experimental data³³ and simulation results for the OPLS model are shown as solid lines and circles, respectively.

interaction site augmented by a square-well potential with an angular dependence that allows only for the formation of dimers.⁴ In contrast, the more realistic molecular-mechanics force field of Briggs et al.²⁴ (see section 3.D) was used in this work. We can take advantage of the simplicity and generality of the AVBMC algorithm, which does not rely on any specific features of the potential energy surface. The bonded V_{in} region was bounded by an inner shell at 2.5 Å and an outer shell at 10 Å based on the carbonyl oxygen-carbonyl oxygen separation, and P_{bias} was set to 0.5. Ten trial sites were considered for the multiple-first-bead insertion^{13,14} of the carbonyl oxygen, and 10 positions, 100 dihedral angles, and 1000 bending angles were sampled at every step of the coupled-decoupled CBMC growth¹⁸ of the remainder of the acetic acid molecule. Using AVBMC in the Gibbs ensemble, there are two types of swap moves: the AVBMC intrabox swap (used only within the vapor phase) and the CBMC interbox swap between the gas and liquid phases. A volume bias was not used for the latter move. The frequencies of the two types of swap moves were adjusted to yield roughly one accepted intrabox swap per 10 Monte Carlo cycles and one accepted interbox swap per 20 cycles (for $T \geq 400$ K) or per 30 cycles (for $T \leq 350$ K). For the intrabox AVBMC move, only accepted $out \rightarrow in$ and $in \rightarrow out$ moves were counted, but the $out \rightarrow out$ and $in \rightarrow in$ moves contribute to the sampling of the gas phase because the maximum translational and rotational displacements were found to be very low.

First of all, for temperatures below $T = 450$ K, relatively long test simulations without the AVBMC moves did not reach equilibrium, i.e., their outcome was dependent on the initial configurations. Thus it is imperative that a special biasing scheme be used to properly calculate the VLCC of acetic acid. The calculated VLCC (using AVBMC) for acetic acid is compared to the experimental data³³ in Figure 13. The OPLS-UA model yields a critical temperature of 685 ± 10 K, much higher than its experimental counterpart of 595 K. The calculated orthobaric vapor densities are significantly too low over the entire temperature range, whereas deviations in the orthobaric liquid densities become more pronounced at the higher temperatures. However, the liquid density at $T = 300$ K is in good

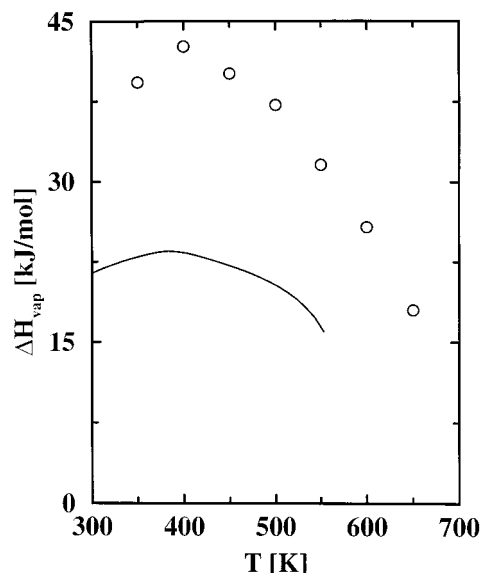


Figure 14. Heats of vaporization for acetic acid versus temperature. Symbols and lines are as in Figure 13.

agreement with experiment, as should be expected because the OPLS-UA model was fitted to liquid densities at 298 and 373 K.²⁴

The heats of vaporization, ΔH_{vap} , are plotted as function of temperature in Figure 14. The OPLS-UA model overestimates ΔH_{vap} by more than 15 kJ/mol over the entire temperature range. This might come as a surprise because the model was fitted to reproduce also the experimental ΔH_{vap} . However, the explanation of this discrepancy is straightforward. Although Briggs et al.²⁴ did not account for the internal energy of the vapor phase in their estimates of ΔH_{vap} , we found that the large extent of clustering (mainly dimers) results in an average nonbonded energy of about -12 kJ/mol for the vapor phase at $T = 350$ K. On the positive side, it is important to note that the OPLS-UA model yields a maximum in ΔH_{vap} at about $T = 400$ K, in good agreement with the experimental data that show a maximum at $T = 383$ K.³³ As for the vapor phase of HF, the maximum in ΔH_{vap} points to a "phase transition" for the acetic acid vapor phase. Finally, it should be pointed out that vapor-phase clusters with three or more molecules were observed in the AVBMC simulations of acetic acid. Again, these configurations can only be sampled using a robust algorithm that does not restrict the types of cluster species.

5. Conclusions

A novel Monte Carlo method, called the aggregation-volume-bias Monte Carlo algorithm, is presented for the efficient sampling of strongly associating fluids. It is demonstrated that the AVBMC algorithm increases computational efficiency by many orders of magnitude compared to unbiased translational and rotational Monte Carlo moves (about 2 orders of magnitude for the vaporizations of the methane droplet and water cluster, and more for the low-temperature vapor phases of hydrogen fluoride and acetic acid, where the unbiased moves did not yield converged results even for very long simulations). Compared to the association-biased Monte Carlo method,^{5,6} the bond-bias Monte Carlo algorithm,⁴ and the monomer-addition-subtraction algorithm,^{7,8} the AVBMC algorithm is simpler, more general, and more robust. Also, it does not require identification of clusters, which greatly reduces the computational overhead compared to nonbiased algorithms. Of particular importance is that the AVBMC algorithm does not rely on any specific details

of the potential energy surface for bonded configurations, and thus the sampling is not restricted to dimeric clusters (as in the BBMC algorithm) or to specific cluster architectures (as in the MASA algorithm). In addition, because an AVBMC move is in fact an intrabox swap move, it can be easily combined with any scheme that improves the sampling of particle insertions/removals (e.g., multiple insertions of the first bead and configurational-bias growth of the remainder of the molecule). As with the BBMC algorithm, extensions of the AVBMC scheme to include interbox swaps (as required for simulations in the grand canonical and Gibbs ensembles) are straightforward. In addition, the AVBMC algorithm can be exploited to sample the spatial distribution of molecules in a network of specific interaction sites, such as acidic sites in zeolites, or in microheterogeneous mixtures, such as alkane-rich solutions of alkanols.

Conventional translational and rotational moves required extremely long equilibration times for the vaporization of the 20-molecule water cluster. In addition, Gibbs ensemble simulations for acetic acid using CBMC interbox swap moves without volume bias did not result in equilibrium configurations even after 10^5 Monte Carlo cycles. These observations might raise some questions on the outcomes of previous Gibbs-ensemble Monte Carlo simulations for methanol³⁴ and dipolar hard spheres³⁵ that did not yield typical vapor–liquid phase equilibria.

Analysis of the AVBMC simulations for the superheated HF vapor phase allows the following conclusions. First of all, there is, in general, very good agreement between the results of the MASA simulations by Visco and Kofke⁸ and the AVBMC simulations reported here. Average association numbers calculated using a macroscopic route (inverse compressibility factors) and using a microscopic distance-based criterion match rather well. From the analysis of cluster distributions, we observe the following: (1) The magnitude of the heat capacity correlates with the change in the fraction of free molecules, and the peak in the heat capacity occurs around the temperature at which about one-half of the HF molecules are not associated. (2) Tetramers and pentamers are the dominant clusters at low temperatures. (3) Branched architectures are important for all HF clusters consisting of four or more molecules.

The vapor–liquid coexistence curve for acetic acid was calculated for the OPLS–UA model. It was found that this model overestimates the critical temperature by about 15%, and the heats of vaporization by about 15 kJ/mol. In addition, the saturated liquid densities are too high at temperatures above 350 K, and the saturated vapor densities are too low over the entire temperature range. Although dimers are the dominant species in the vapor phase, larger clusters were also observed.

Acknowledgment. Financial support from the National Science Foundation (CTS–9813601), a Sloan Research Fellowship, and a Doctoral Dissertation Fellowship (B.C.) is gratefully acknowledged. Part of the computer resources were provided by the Minnesota Supercomputing Institute.

Appendix: Generation of Trial Sites in the V_{in} or V_{out} Regions

Two methods can be used to generate trial sites in the V_{in} region. The selection of one of these two methods depends on the ratio of the inner-shell and outer-shell distances (r_{below} and r_{above} that bound the V_{in} region). If $r_{\text{below}} \ll r_{\text{above}}$, then the generation of a trial site proceeds as follows: (1) A trial site is randomly placed within a cube centered at the target particle j and with a linear dimension equal to r_{above} . (2) If this trial site is outside the bonded region (i.e., toward the edges of the cube), the process is repeated until an appropriate site is found.

If $r_{\text{below}} < r_{\text{above}}$, then the generation of a trial site proceeds as follows: (1) Generate a unit vector distributed uniformly on the unit sphere following the description in ref 2. (2) Scale the unit vector with a factor calculated from $[\xi(r_{\text{above}}^3 - r_{\text{below}}^3 + r_{\text{below}}^3)]^{1/3}$, where ξ is a random number uniformly distributed between 0 and 1. (3) Add the scaled vector to the position vector of target particle j .

To swap into the *out* volume, the particle is randomly placed anywhere in the simulation box (the system volume V). If this site happens to be within the bonded region of the target particle j , then the process is repeated until an appropriate site is found.

If multiple first-bead insertions are used, then the generation of a trial site in the V_{in} or V_{out} regions (as described above) is carried out multiple times to give the required number of trial sites.

References and Notes

- (1) Prausnitz, J. M. *Molecular Thermodynamics of Fluid-Phase Equilibria*, 2nd ed.; Prentice Hall: Englewood Cliffs, NJ, 1986.
- (2) Allen, M. P.; Tildesley, D. J. *Computer Simulations of Liquids*; Oxford University Press: Oxford, 1987.
- (3) Metropolis, N.; Rosenbluth, A. W.; Rosenbluth, M. N.; Teller, A. H.; Teller, E. *J. Chem. Phys.* **1953**, *21*, 1087.
- (4) Tsangaris, D. M.; de Pablo, J. J. *J. Chem. Phys.* **1994**, *101*, 1477.
- (5) Busch, N. A.; Wertheim, M. S.; Chiew, Y. C.; Yarmush, M. L. *J. Chem. Phys.* **1994**, *101*, 3147.
- (6) Busch, N. A.; Wertheim, M. S.; Yarmush, M. L. *J. Chem. Phys.* **1996**, *104*, 3962.
- (7) Visco, D. P., Jr.; Kofke, D. A. *J. Chem. Phys.* **1998**, *109*, 4015.
- (8) Visco, D. P., Jr.; Kofke, D. A. *J. Chem. Phys.* **1999**, *110*, 5493.
- (9) McQuarrie, D. A. *Statistical Mechanics*; Harper & Row: New York, 1976.
- (10) The extent (diameter) of the bonded region must be defined before the AVBMC simulation can be carried out; it remains fixed throughout the simulation. For hydrogen-bonding fluids, the bonded regions can be defined as the maximum hydrogen-bond distance (between the heavy atoms) and can be estimated a priori from energetic considerations or be determined from radial distribution functions calculated over short test simulations. See also the Appendix.
- (11) Siepmann, J. I.; McDonald, I. R. *Mol. Phys.* **1992**, *75*, 255.
- (12) Stubbs, J. M.; Chen, B.; Potoff, J. J.; Siepmann, J. I. *Fluid Phase Equilib.*, submitted for publication.
- (13) Esselink, K.; Loyens, L. D. J. C.; Smit, B. *Phys. Rev. E* **1995**, *51*, 1560.
- (14) Mackie, A. D.; Tavittian, B.; Boutin, A.; Fuchs, A. H. *Mol. Simul.* **1997**, *19*, 1.
- (15) Siepmann, J. I.; Frenkel, D. *Mol. Phys.* **1992**, *75*, 59.
- (16) Frenkel, D.; Mooij, G. C. A. M.; Smit, B. *J. Phys.: Condens. Matter* **1992**, *4*, 3053.
- (17) de Pablo, J. J.; Laso, M.; Suter, U. W. *J. Chem. Phys.* **1992**, *96*, 2395.
- (18) Martin, M. G.; Siepmann, J. I. *J. Phys. Chem. B* **1999**, *103*, 4508.
- (19) Wick, C. D.; Siepmann, J. I. *Macromolecules*, in press.
- (20) Martin, M. G.; Siepmann, J. I. *J. Phys. Chem. B* **1998**, *102*, 2569.
- (21) Berendsen, H. J. C.; Grigera, J. R.; Straatsma, T. P. *J. Phys. Chem.* **1987**, *91*, 6269.
- (22) Courmoyer, M. E.; Jorgensen, W. L. *Mol. Phys.* **1984**, *51*, 119.
- (23) McDonald, I. R. *Mol. Phys.* **1972**, *23*, 41.
- (24) Briggs, J. M.; Nguyen, T. B.; Jorgensen, W. L. *J. Phys. Chem.* **1991**, *95*, 3315.
- (25) Panagiotopoulos, A. Z. *Mol. Phys.* **1987**, *61*, 813.
- (26) Panagiotopoulos, A. Z.; Quirk, N.; Stapleton, M.; Tildesley, D. J. *Mol. Phys.* **1988**, *63*, 527.
- (27) Vlugt, T. J. H.; Martin, M. G.; Smit, B.; Siepmann, J. I.; Krishna, R. *Mol. Phys.* **1998**, *94*, 727.
- (28) Suhm, M. A. *Ber. Bunsen-Ges. Phys. Chem.* **1995**, *99*, 1159.
- (29) Frank, E. U.; Meyer, F. Z. *Elektrochem.* **1959**, *63*, 571.
- (30) Wu, D.; Chandler, D.; Smit, B. *J. Phys. Chem.* **1992**, *96*, 4077.
- (31) Curtiss, L. A.; Blander, M. *Chem. Rev.* **1988**, *88*, 827.
- (32) Sear, R. P.; Jackson, G. J. *Chem. Phys.* **1996**, *105*, 1113.
- (33) Vargaftik, N. B. *Handbook of Physical Properties of Liquids and Gases: Pure Substances and Mixtures*, 2nd ed.; Hemisphere: Washington, DC 1983.
- (34) van Leeuwen, M. E. *Mol. Phys.* **1996**, *87*, 87.
- (35) van Leeuwen, M. E.; Smit, B. *Phys. Rev. Lett.* **1993**, *71*, 3991.